

A study on blast-loaded aluminium plates with crack-like defects subjected to blast loading

Henrik Granum¹, David Morin^{2,3}, Tore Børvik^{2,3}, Odd Sture Hopperstad^{2,3}

¹Enodo AS, Trondheim, Norway

²Structural Impact Laboratory (SIMLab), Department of Structural Engineering, Norwegian University of Science and Technology (NTNU), Trondheim, Norway

³Centre for Advanced Structural Analysis (CASA), NTNU, Trondheim, Norway

Abstract

*This paper presents a study on AA6016 plates in temper T4 subjected to blast loading. Four different crack-like defects have been introduced in the plates to facilitate crack propagation as the dominating failure mode. Uniaxial tensile specimens extracted from a plate are used in the calibration of the *MAT_258 material model available in LS-DYNA. This material model contains a non-quadratic yield surface, isotropic work hardening and a failure model where the onset of failure is dependent on the element size as well as its bending-to-membrane loading ratio. Four different element sizes are investigated to assess the ability of the model to predict the onset of failure and subsequent crack propagation in blast-loaded plates by comparison to experiments conducted in a shock tube facility.*

1 Introduction

Finite element (FE) simulations of thin-walled structural components predominantly use shell elements due to versatile formulation and computational efficiency. The elastic-plastic domain is accurately predicted by shell elements, yet local necking is difficult to represent correctly. Usually, the element size is much larger than the width of the neck, evening out the strain gradient. At the onset of necking, the stress state changes from a plane stress state to a three-dimensional stress state, which the shell element formulation is unable to represent. When a shell element is subjected to pure bending, the element will not experience necking, resulting in higher ductility than in membrane-dominated problems where necking occurs. This must be kept in mind when modeling a component subjected to mixed loading. As a result, shell elements are generally considered unsuitable to model failure and crack propagation.

Multiple attempts have been made to overcome the mentioned challenges [1-2], where the *MAT_258 [3-4] material model is one of them. Here, the fracture parameter is computed as a function of the element size. In addition, it treats fracture due to stretching and bending separately, enabling the onset of fracture to be predicted for both bending and membrane-dominated problems. In this study, *MAT_258 is calibrated based on a single uniaxial tension test and used in simulations of thin plates with crack-like defects subjected to blast loading. The results are qualitatively compared to experiments conducted in a shock tube facility.

2 Material and material tests

The rolled plates were made of aluminium alloy AA6016 in temper T4 manufactured by Hydro Aluminium Rolled Products in Bonn, Germany. They were delivered with in-plane dimensions 625 mm × 625 mm and a thickness of 1.5 mm. This is a medium strength alloy with good corrosion resistance, often used by the automotive industry in car-body components subjected to paint-bake cycles. The chemical composition of the alloy is given in Table 1.

Table 1: Chemical composition of AA6016 in wt%.

| Si | Mg | Fe | Cu | Mn | Cr | Zn | Ti | Al |
|--------|--------|--------|--------|--------|--------|--------|--------|---------|
| 1.3160 | 0.3490 | 0.1617 | 0.0081 | 0.0702 | 0.0025 | 0.0084 | 0.0175 | Balance |

Uniaxial tensile specimens were extracted from a plate in the 0°, 45° and 90° directions with respect to the rolling direction. The specimen had a gauge length, width and thickness of 70 mm, 12.5 mm, and 1.5 mm, respectively. Figure 1a shows the specimen geometry. The material tests were conducted in an Instron 5982 universal testing machine with a crosshead velocity of 0.035 mm/s, corresponding to an initial strain rate of 0.0005 1/s. A black and white speckle pattern was applied to the in-plane surface

of the gauge prior to testing. A camera oriented perpendicular to the specimen recorded images of the tests at 1 Hz. Digital image correlation (DIC) analyses were performed, where a 50 mm long virtual extensometer was used to calculate the engineering strain. The engineering stress was calculated based on the force recorded by the load cell attached to the test machine. Representative engineering stress-strain curves from the tests in the three directions with respect to the rolling direction are shown in Figure 1b along with the simulation with the calibrated material model. The representative test from the rolling direction is used in the calibration of the material model presented in Section 4.

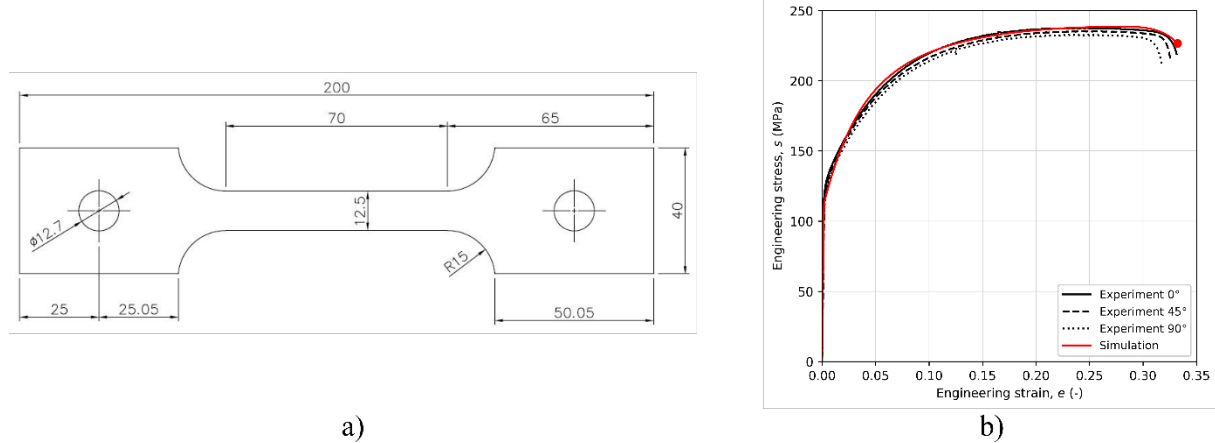


Figure 1: a) Geometry of the UT200 specimen with measurements in mm, and b) representative engineering stress-strain curves from the tension tests with extensometer length $L = 50$ mm.

3 Blast tests

The blast tests were conducted in a shock tube facility at NTNU and are part of a larger study presented in Granum et al. [5-6]. A detailed description and evaluation of the shock tube facility can be found in Aune et al. [7] and only a brief overview is given in the following. The shock tube has a total length of approximately 17 m with an inner diameter of 0.331 m. To begin the test, a chamber in one end of the tube is filled with compressed air, separated from the rest of the tube by diaphragms. When the targeted pressure is reached, a ventilating process initiates which ruptures the diaphragms, resulting in a blast wave traveling towards the plate mounted in the other end of the tube. The cross-section of the tube gradually transforms from a circular to a square cross-section area, giving a blast-exposed area of 300 mm \times 300 mm. The test plate was clamped to the flange of the tube by use of two clamping frames.

Prior to testing the plates, four different crack-like defects were machined by use of wire erosion. The geometry of the blast-exposed area of the four different plates (B-1 to B-4) is shown in Figure 2. The peak pressure in the pressure-times history of the blast wave was approximately 600 kPa. Two synchronized Phantom v1610 high-speed cameras positioned in a stereovision setup recorded the blast event at 24 000 fps with an image resolution of 768 \times 800 pixels.

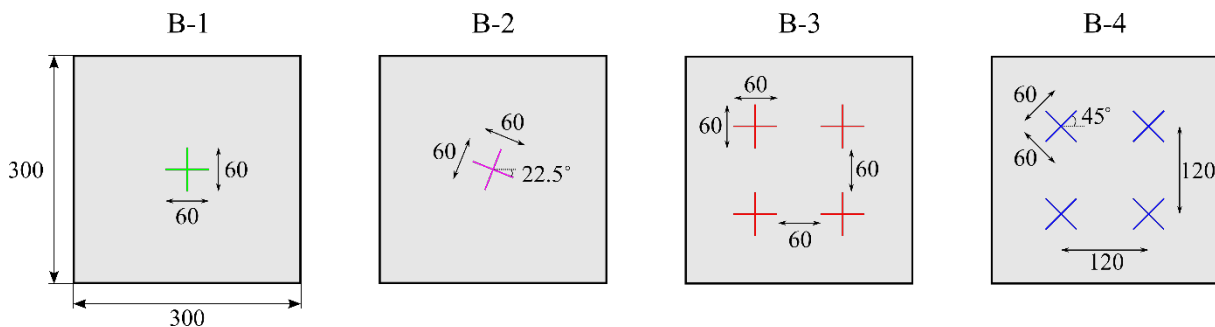


Figure 2: Geometry of the blast-exposed area of the four different initial defect geometries. Measurements are in mm.

4 Material modelling

The ***MAT_258** (***MAT_NON_QUADRATIC_FAILURE**) material model in LS-DYNA was used in the numerical simulations. It consists of a non-quadratic yield surface [8-9] and a modified Johnson-Cook type of viscoplastic relation [10]. In this study, a rate-independent formulation was selected due to the

low strain rate sensitivity reported for 6xxx-series aluminium alloys [11] at room temperature. Failure is governed by the Cockcroft-Latham (CL) failure criterion [12] and is uncoupled from the constitutive relation. However, both the deformation mode and element size are accounted for in this version of the failure model. The equivalent stress is defined as

$$\bar{\sigma}_{\text{eq}} = \left[\frac{1}{2} (|\sigma_1 - \sigma_2|^a + |\sigma_2 - \sigma_3|^a + |\sigma_3 - \sigma_1|^a) \right]^{\frac{1}{a}} \quad (1)$$

where $\sigma_1 > \sigma_2 > \sigma_3$ are the ordered principal stresses and a controls the curvature of the yield surface. For face centred cubic materials like aluminium alloys, $a = 8$ have been suggested based on polycrystal plasticity simulations [13]. The hardening curve is defined by a three-term Voce hardening rule on the form

$$\sigma_Y = \sigma_0 + R(\bar{\varepsilon}^p) = \sigma_0 + \sum_{i=1}^3 Q_i \left(1 - \exp\left(-\frac{\theta_i}{Q_i} \bar{\varepsilon}^p\right) \right) \quad (2)$$

Here, σ_0 is the initial yield stress, Q_i and θ_i are hardening parameters controlling the work hardening and $\bar{\varepsilon}^p$ is the equivalent plastic strain. Failure is modelled by the CL failure criterion, where the damage variable D is defined as

$$D = \frac{1}{W_C} \int \langle \sigma_1 \rangle d\bar{\varepsilon}^p \leq 1 \quad (3)$$

In Eq. (3), W_C is the fracture parameter and $\langle \cdot \rangle$ is the Macaulay brackets: $\langle x \rangle = \max(0, x)$. Fracture occurs for $D = D_C = 1$. The deformation-mode dependence is accounted for by defining the fracture parameter W_C as

$$W_C = \Omega W_C^b + (1 - \Omega) W_C^m \quad (4)$$

where Ω is a deformation mode indicator, W_C^b is the fracture parameter in pure bending, and W_C^m is the fracture parameter in pure membrane loading. By this relation, $\Omega = 1$ represents pure bending and $\Omega = 0$ represents pure membrane loading. Figure 3 illustrates the effect of the bending-to-membrane ratio on the equivalent plastic strain at failure. The deformation indicator is defined by the through-thickness plastic strains as

$$\Omega = \frac{1}{2} \frac{|\varepsilon_{33}^{p+} - \varepsilon_{33}^{p-}|}{\max(|\varepsilon_{33}^{p+}|, |\varepsilon_{33}^{p-}|)} \quad (5)$$

where ε_{33}^{p+} and ε_{33}^{p-} are the through-thickness plastic strains in the two outermost integration points of the shell element. The effect of element size is accounted for in the membrane fracture parameter (W_C^m), whereas the bending fracture parameter (W_C^b) is identical for all element sizes. The membrane fracture parameter is expressed as a function of the element's aspect ratio l_e/t_e , where l_e and t_e are the element length and thickness, respectively, and reads

$$W_C^m = W_C^l + (W_C^s - W_C^l) \exp\left(-c \left(\frac{l_e}{t_e} - 1\right)\right) \quad (6)$$

In Eq. (6), W_C^l , W_C^s and c are model parameters to be calibrated.

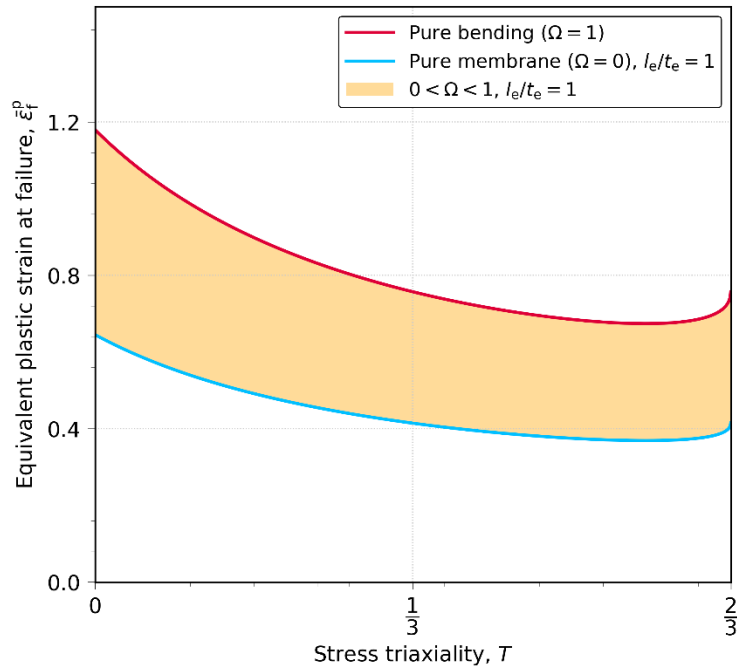


Figure 3: The effect of the deformation mode indicator on the equivalent plastic strain at failure.

The material model was calibrated by a similar approach as described in Holmen et al. [14] and only a condensed overview is given here. The material model was calibrated solely based on the representative test in the rolling direction of the plate, following these steps:

1. Hardening parameters (σ_0, Q_i, θ_i): A virtual extensometer of length 50 mm was used to extract the elongation and calculate the engineering stress-strain curve of a test by means of DIC. LS-OPT analyses with a solid element model of the tension test were run, where the measured stress-strain curve was used as target curve. The calibrated hardening parameters were found when the optimal set of model parameters was given by LS-OPT using a mean squared error between the simulated curve and the target curve.
2. Bending fracture parameter (W_C^b): The fracture parameter governing bending was obtained by integrating the major principal stress over the equivalent plastic strain obtained from the through-thickness centre integration point from a simulation of a tensile test with a fine solid element mesh. The equivalent plastic strain at fracture was determined based on the onset of failure in the test, indicated by the red circle Figure 1b.
3. Membrane fracture parameter (W_C^m) and corresponding model parameters (W_C^l, W_C^s, c): Shorter virtual extensometers spanning across the neck were used to extract elongations by DIC. These elongations were then applied as boundary conditions in single-element simulations of uniaxial tension until the onset of fracture in the test. Fracture parameters for different extensometer lengths were found by numerical integration. The optimized model parameters were found by a curve fit of Eq. (4) to the fracture parameters for different extensometer lengths.

The material constants and model parameters of the calibrated model are given in Table 2 and Table 3.

Table 2: Material constants and work hardening parameters.

| ρ (kg/m ³) | E (MPa) | ν | σ_0 (MPa) | θ_1 (MPa) | Q_1 (MPa) | θ_2 (MPa) | Q_2 (MPa) | θ_3 (MPa) | Q_3 (MPa) | a |
|--------------------------------|--------------|-------|---------------------|---------------------|----------------|---------------------|----------------|---------------------|----------------|-----|
| 2700 | 70 000 | 0.3 | 112.46 | 2579.60 | 78.64 | 542.06 | 109.80 | 163.57 | 325.69 | 8 |

Table 3: Failure parameters for *MAT_258.

| D_C | W_C^b (MPa) | W_C^l (MPa) | W_C^s (MPa) | ϕ | γ | c |
|-------|------------------|------------------|------------------|--------|----------|-------|
| 1.0 | 245.22 | 79.05 | 116.11 | 1.0 | 1.0 | 0.361 |

5 Numerical results

5.1 Finite element modelling

The numerical simulations of the blast-loaded plates were conducted in the explicit solver of LS-DYNA. Only the blast-exposed area of the plate was modelled where the edge was fixed to mimic the boundary conditions applied by the clamping frames in the shock tube. Four different mesh densities were used in the simulations, represented by their different length-to-thickness ratios, $l_e/t_e = 0.33, 1, 3,$ and 5 . This resulted in approximately 450 000 elements for the smallest length-to-thickness ratio and below 2000 elements for the largest ratio. Shell elements with reduced integration and five integration points through the thickness were used in all simulations (ELFORM = 2 in LS-DYNA). The blast loading was applied as a pressure load. The pressure-time history was taken from a test conducted by Aune et al. [7] under similar test conditions, where it was measured by a pressure sensor mounted on the surface of a rigid plate. Element erosion was used to model failure, setting the stress tensor to zero in all integration points when the damage variable D reached unity.

5.2 Blast simulations

In all experiments, the plates were seen to deform as a petal originating from the crack-like defects. This type of failure mode results in significantly in-plane rotations around the defects as the plate is deformed by the blast load. By applying the blast load as a pressure load in the simulation, the pressure direction will always coincide with the normal of the shell, regardless of how the elements deform. Due to the in-plane rotations of the plate during a test, one may end up in a situation where the pressure acts in the opposite direction to the initial loading direction. This can lead to exaggerated rotations in the simulations which again affects the crack initiation and propagation. To prevent this unwanted effect, a user-defined subroutine was implemented, where the magnitude of the pressure is multiplied by the cosine of the angle between the initial load direction and the normal to the shell element. As the element rotates, the magnitude of the pressure is gradually decreased, allowing the pressure to “slide off”. A laser scanner was used to acquire 3D-models of the tested plates. Figure 4 shows a side view of the B-1 experiment and simulations where the two pressure formulations have been employed. Based on this and similar figures, the deformation pattern obtained with the user-defined pressure formulation is found to be in much better agreement with the experimental results than with the standard formulation. Thus, the user-defined pressure formulation was used in the rest of this study.

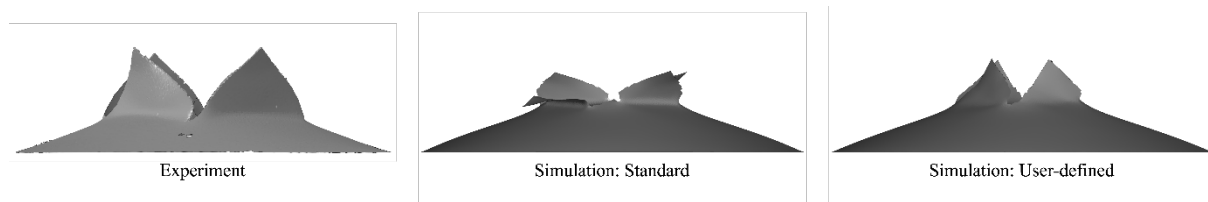


Figure 4: Side view of the B-1 experiment and simulation with standard and user-defined pressure formulation.

In Figure 5, image series from the B-2 experiment and corresponding simulations with different length-to-thickness ratios are shown at selected points in time. The time points range from $t = 0.50$ ms to $t = 2.00$ ms, where $t = 0$ ms indicates the time of impact by the blast wave. From the image series of the B-2 experiment, one can see that a petal deformation develops at the crack-like defects and cracks propagate towards the corners of the plate. As expected, the discretization of the plate plays a vital role when modelling failure and crack propagation. For the coarsest element size ($l_e/t_e = 5$) the damage is spread over such large elements that failure does not initiate. When decreasing the length-to-thickness ratio, better accuracy of the deformation pattern is obtained, yet only the finest element size ($l_e/t_e = 0.33$) can predict a similar crack propagation as seen in the experiment. Crack propagation is in general problematic with element erosion, as removing an element introduces a significantly blunter crack than in the experiment. However, the simulations with the two smallest element sizes ($l_e/t_e = 0.33$ and $l_e/t_e = 1$) both give acceptable results in this study.

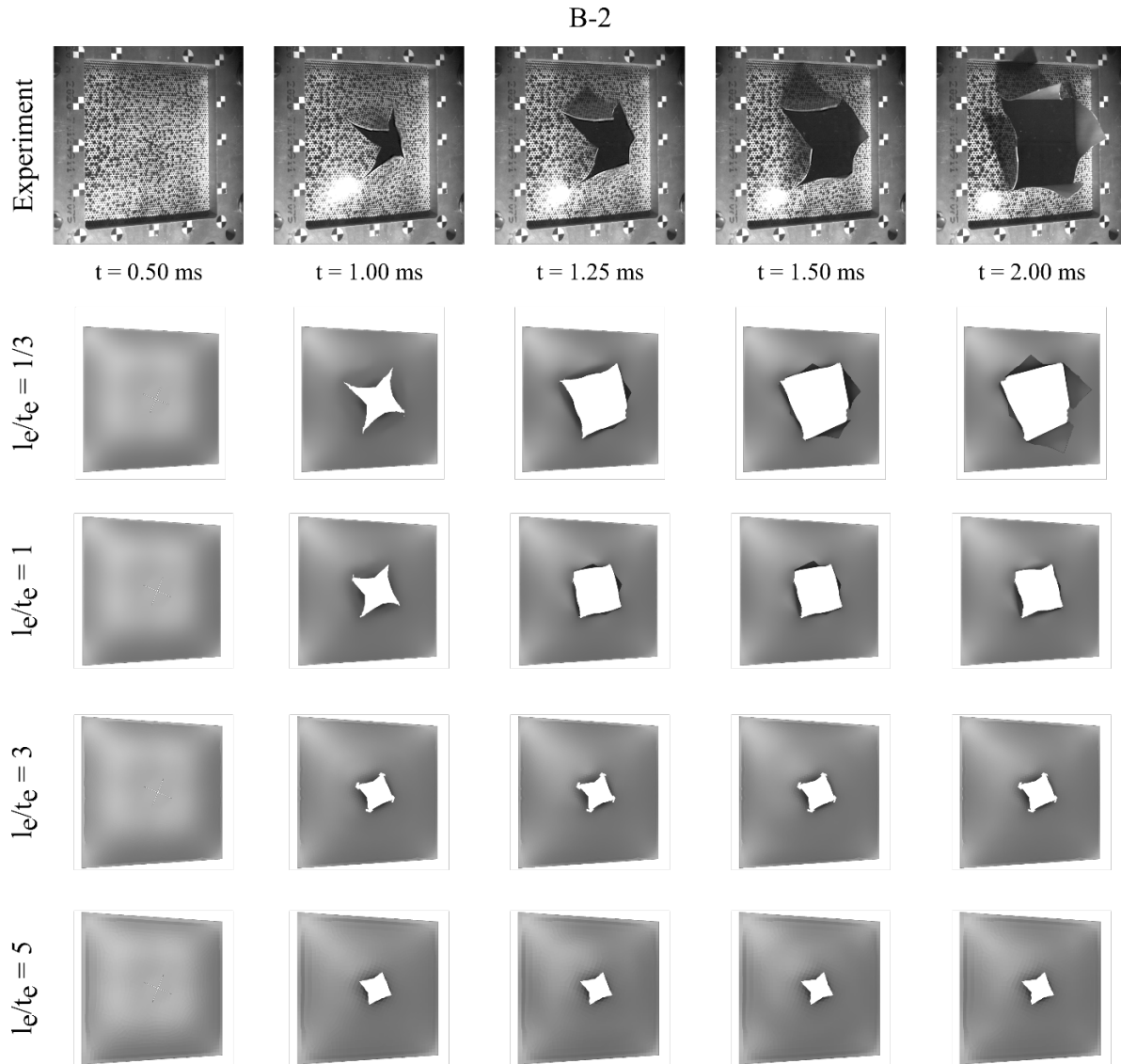


Figure 5: Image series from the B-2 test and corresponding simulations with different length-to-thickness ratios at selected points in time.

A comparison of the tests of the four plates and simulations with different length-to-thickness ratios at $t = 2.00$ ms is shown in Figure 6. The overall trends are the same as seen for the B-2 test in Figure 5, where the simulations with the two smallest length-to-thickness ratios ($l_e/t_e = 0.33$ and $l_e/t_e = 1$) give acceptable results. The correct failure pattern is predicted for the tests B-1 to B-3 with these length-to-thickness ratios, showing the capabilities of the FE models and the material model. In the simulation of the B-4 test with the finest mesh, the correct crack pattern is initiated but suddenly arrested. Instead, cracks propagate between the edges of the defects pointing towards the centre of the plate. The simulation with $l_e/t_e = 1$ of the B-4 test is not well predicted, where the cracks were arrested too early while propagating towards the diagonals of the plate. Based on the results in Figure 6, the simulations with the two coarsest element sizes ($l_e/t_e = 3$ and $l_e/t_e = 5$) are not suitable to capture either failure initiation or crack propagation.

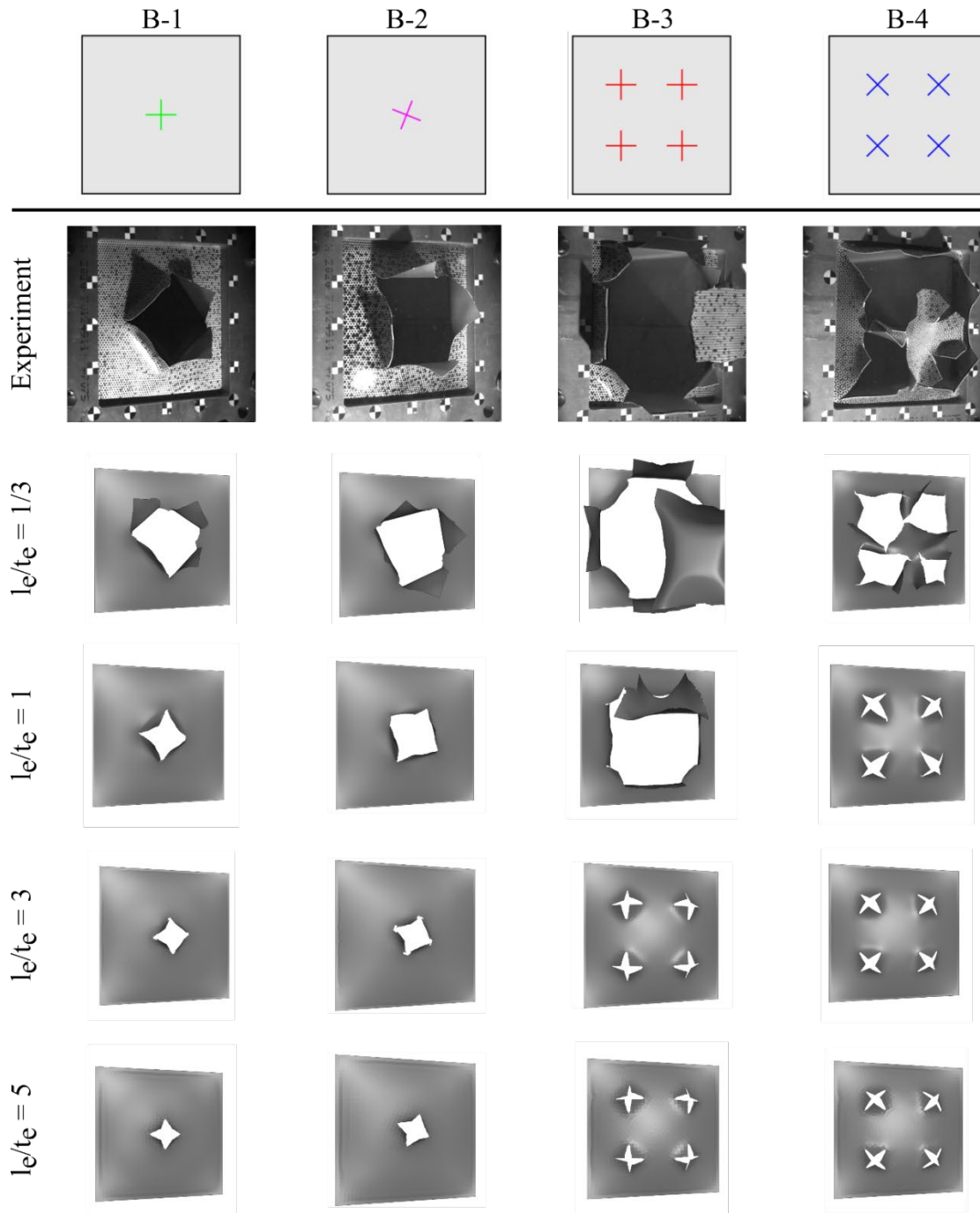


Figure 6: Comparison of tests and simulations with different length-to-thickness ratios at $t = 2.00$ ms.

A contour plot of the deformation mode indicator (Ω) defined in Eq. (5) is shown in Figure 7 for simulations with $l_e/t_e = 1$ at $t = 1.25$ ms. The loading is membrane-dominated, but around the corners of the plates and at the defects, areas with mixed loading conditions are seen. As expected, such a thin plate has limited bending stiffness when compared to the membrane capacity. However, considering that the cracks propagate from the defects where the loading conditions are mixed, the importance of including a failure model that accounts for the difference in ductility depending on the loading conditions becomes apparent.

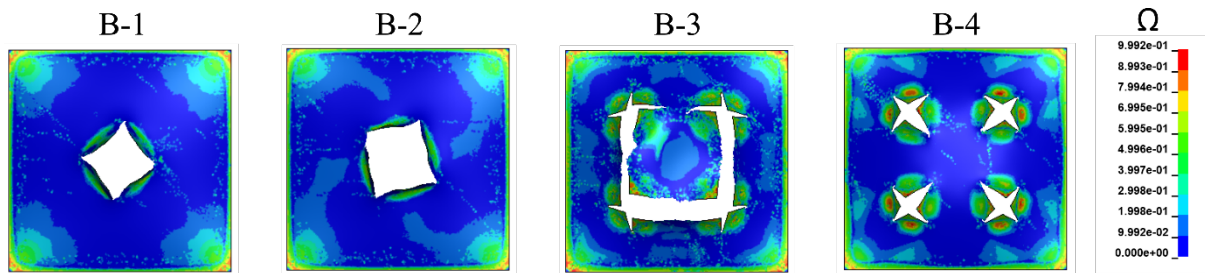


Figure 7: Contour plots of the deformation mode indicator Ω for simulations with $l_e/t_e = 1$ at $t = 1.25$ ms.

6 Conclusions

In this work, the behaviour of AA6016-T4 aluminium plates with crack-like defects subjected to blast loading has been investigated using experimental tests and LS-DYNA simulations. The finite element model consisted of the blast-exposed area of the plate with four different length-to-thickness ratios of the element size, employing a user-defined subroutine to apply the blast loading. The ***MAT_258** (***MAT_NON_QUADRATIC_FAILURE**) material model was employed, consisting of a high-exponent yield surface, isotropic hardening, and an uncoupled failure model with through-thickness damage regularization. Based on the results, a length-to-thickness ratio of the element equal to unity ($l_e/t_e = 1$) was found sufficient to describe the onset of failure in the simulations of the four tests. However, to predict both the onset of failure and subsequent crack propagation in all but the B-4 test correctly, the smallest element size ($l_e/t_e = 0.33$) is necessary. Considering that the material model is calibrated based on a single uniaxial tensile test, the ability of the model to predict both failure and crack propagation is good if the geometry is sufficiently discretized.

Acknowledgment

This study was conducted as part of the PhD-work of Henrik Granum at NTNU. Financial support came from NTNU, and the Research Council of Norway through the FRINATEK Programme, Project No. 250553 (FractAI).

Literature

- [1] Woelke PB, Shields MD, Abbound NN, Hutchinson JW. "Simulations of ductile fracture in an idealized ship grounding scenario using phenomenological damage and cohesive zone models". *Computational Materials Science* 80, 2013, 79-95.
- [2] Pack K, Mohr D. "Combined necking & fracture model to predict ductile failure with shell finite elements". *Engineering Fracture Mechanics* 182, 2017, 32-51.
- [3] Costas M, Morin D, Hopperstad OS, Børvik T, Langseth M. "A through-thickness damage regularization scheme for shell elements subjected to severe bending and membrane deformations". *Journal of the Mechanics and Physics of Solids* 123, 2019, 190-206.
- [4] Livermore Software Technology Corporation (LSTC). *LS-DYNA Keywords User's Manual*.
- [5] Granum H, Aune V, Børvik T, Hopperstad OS. "Effect of heat-treatment on the structural response of blast-loaded aluminium plates with pre-cut slits". *International Journal of Impact Engineering* 132, 2019, 103306.
- [6] Granum H, Morin D, Børvik T, Hopperstad OS. "Simulation of blast-loaded aluminium plates with crack-like defects". 10th National Conference on Computational Mechanics – MekIT'19, Trondheim, Norway, 2019.
- [7] Aune V, Fagerholt E, Langseth M, Børvik T. "A shock tube facility to generate blast loading on structures". *International Journal of Protective Structures* 6, 2016, 340-366.
- [8] Hershey AV. "The plasticity of an isotropic aggregate of anisotropic face-centered cubic crystals". *Journal of Applied Mechanics* 76, 1954, 241-249
- [9] Hosford WF. "A generalized isotropic yield criterion". *Journal of Applied Mechanics* 39, 1972, 607-609.
- [10] Børvik T, Hopperstad OS, Berstad T, Langseth M. "A Computational model of viscoplasticity and ductile damage for impact and penetration". *European Journal of Mechanics – A/Solids* 20, 2001, 685-712.

- [11] Vilamosa V, Clausen AH, Børvik T, Skjervold SR, Hopperstad OS. «Behaviour of Al-Mg-Si alloys at a wide range of temperatures and strain rates». International Journal of Impact Engineering 86, 2015, 223-239.
- [12] Cockcroft M, Latham D. "Ductility and workability of metals". Journal of the Institute of Metals 1968, 33-39.
- [13] Hosford WF. "On the crystallographic basis of yield criterion". Textures and Microstructures 26-27, 1996, 479-493.
- [14] Holmen JK, Johnsen J, Morin D, Børvik T, Langseth M. "Application of *MAT_258 for bending and crushing of extruded aluminium profiles using shell elements". 16th International LS-DYNA Users Conference. Detroit, USA. 2020.